ADVANCED ENERGY MATERIALS
www.advenergymat.de

Oxygen-Induced Structural Disruption for Improved Li^+ Transport and Electrochemical Stability of Li_3PS_4

*Michael J. Deck, Po-Hsiu Chien, Tej P. Poudel, Yongkang Jin, Haoyu Liu, and Yan-Yan Hu**

The performance of all-solid-state batteries (ASSBs) relies on the Li^+ transport and stability characteristics of solid electrolytes (SEs). Li_3PS_4 is notable for its stability against lithium metal, yet its ionic conductivity remains a limiting factor. This study leverages local structural disorder via O substitution to achieve an ionic conductivity of 1.38 mS cm^{-1} with an activation energy of 0.34 eV for $Li_3PS_{4-x}O_x$ ($x = 0.31$). Optimal O substitution transforms Li^+ transport from 2D to 3D pathways with increased ion mobility. $Li_3PS_{3.69}O_{0.31}$ exhibits improvements in the critical current density and stability against Li metal and retains its electrochemical stability window compared with Li_3PS_4. The practical implementation of $Li_3PS_{3.69}O_{0.31}$ in ASSBs half-cells, particularly when coupled with TiS_2 as the cathode active material, demonstrates substantially enhanced capacity and rate performance. This work elucidates the utility of introducing local structural disorder to ameliorate SE properties and highlights the benefits of strategically combining the inherent strengths of sulfides and oxides via creating oxysulfide SEs.

1. Introduction

The current generation of rechargeable lithium-ion batteries (LIBs) is widely used in applications, such as consumer electronics, electric vehicles, and aerospace. However, due to safety hazards associated with flammable liquid-electrolytes (LEs) and the increased need for high energy densities, all-solid-state lithium batteries (ASSBs) have emerged as a favorable option.[1,2] ASSBs enable greater energy density by allowing dense packing and exhibit improved performance at high temperatures due to the thermal stability of solid electrolytes (SEs).[2–4] SEs are the cornerstone of ASSBs, and some can now achieve ionic conductivities higher than that of LEs[5] by creating a flattened (frustrated) energy landscape via leveraging local structural disorder.[6–11]

In particular, oxysulfide SEs show versatility in tuning their ionic conductivity, mechanical properties, and stability.[12–22] The intrinsically high ionic conductivity of sulfides can be further increased through introducing local structural disorder using S→O substitution and benefit from the chemical stability of O-based SEs. For example, Sun et al. enhanced cycling performance while retaining high ionic conductivity in $Li_{10}GeP_2S_{12-x}O_x$ ($0 \leq x < 0.9$).[23] Additionally, reports on $Li_{3.35}P_{0.93}S_{3.5}O_{0.5}$ and $Li_6PS_{4.75}ClO_{0.25}$ highlighted the advantages of oxysulfide SEs by reducing the solid-electrolyte-interphase (SEI) resistance.[20,21] Furthermore, $Li_{10}SiP_2S_{11.3}O_{0.7}$ exhibited increased ionic conductivity via introducing a crystalline $PS_{4-x}O_x$ unit.[24]

As the parent compound to the lithium superionic conductor (thio-LISICON) class of SEs,[25] Li_3PS_4 has attracted immense interest due to its low cost, chemical stability, and reduced reactivity against Li metal, in comparison to other sulfide-based SEs.[26,27] However, the low ionic conductivity ($\sigma = 10^{-7}$–10^{-4} S cm^{-1}) limits its commercial use in ASSBs.[28,29] To make Li_3PS_4 commercially viable in ASSBs, avenues for improving its properties without substantially raising production costs need to be investigated. In addition to enhancing its ionic conductivity, it is necessary to further stabilize the Li|Li_3PS_4 interface. One promising approach is to introduce O into Li_3PS_4. Experimental results by Gobet et al. of Li_3PS_4 solvent-assisted synthesis indicated that S→O exchange could occur between the solvent (tetrahydrofuran) and PS_4^{3-} to form oxysulfide $(PS_{4-x}O_x)^{3-}$,[30] which stabilizes the higher conducting β-allotrope of Li_3PS_4 thereby enhancing the Li^+ conductivity of Li_3PS_4 ($\sigma_{25\,°C} = 0.1$ mS cm^{-1}).[30,31] Recent computational work has indicated ionic conductivity enhancements of β-Li_3PS_4 via O substitution.[12,25,32,33] A critical O amount of $x = 0.25$ in β-$Li_3PS_{4-x}O_x$ has been suggested to improve Li^+ transport due to flattening the potential energy surface via diversifying the Li chemical environments, leading to changing from quasi-2D to 3D Li^+ diffusion while maintaining its electrochemical stability window.[12,25,32] However, experimental efforts have yet to validate these computational claims and to determine the optimal amount of $PS_{4-x}O_x$ structural units in $Li_3PS_{4-x}O_x$. Moreover, the intrinsic redox-active nature of sulfide SEs and their redox products, capable of generating additional capacity in ASSBs, can be beneficial in improving energy density. Notably, this aspect has not been experimentally investigated for lithium oxysulfides.[34–38]

M. J. Deck, T. P. Poudel, Y. Jin, H. Liu, Y.-Y. Hu
Department of Chemistry and Biochemistry
Florida State University
95 Chieftan Way, Tallahassee, FL 32306, USA
E-mail: yhu@fsu.edu
P.-H. Chien, Y.-Y. Hu
Center of Interdisciplinary Magnetic Resonance
National High Magnetic Field Laboratory
1800 East Paul Dirac Drive, Tallahassee, FL 32310, USA

The ORCID identification number(s) for the author(s) of this article can be found under https://doi.org/10.1002/aenm.202302785

DOI: 10.1002/aenm.202302785

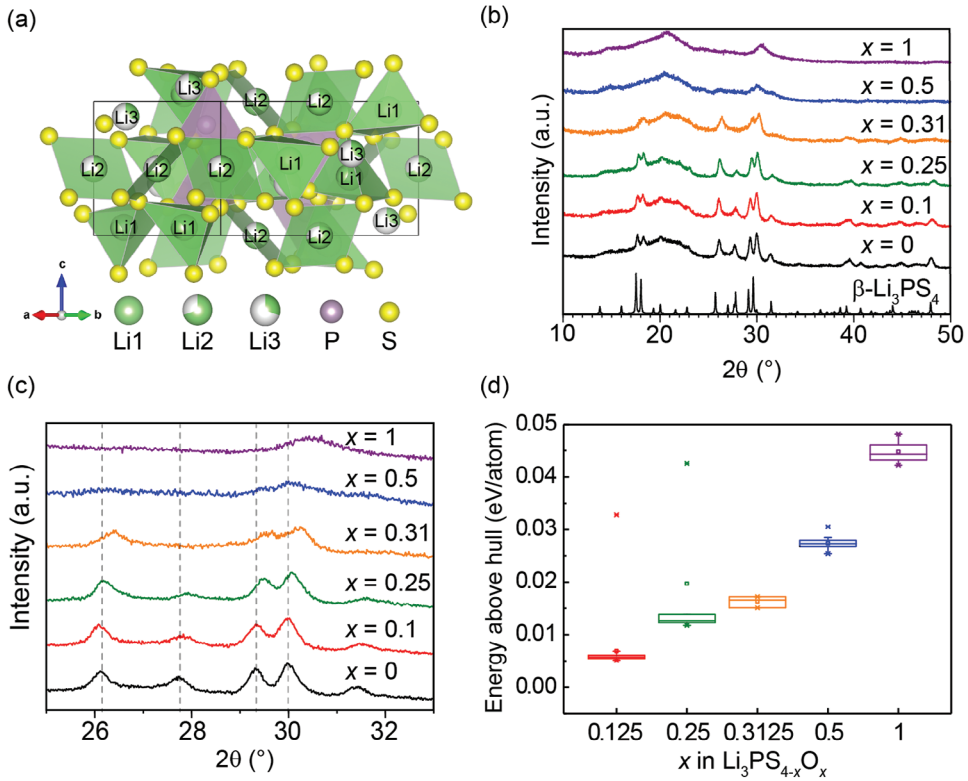

Figure 1. a) Crystal structure of β-Li_3PS_4 (ICSD #180319). b) PXRD patterns of $Li_3PS_{4-x}O_x$ ($x = 0$, 0.1, 0.25, 0.31, 0.5, and 1) and β-Li_3PS_4 (ICSD #180319). Broad Kapton film background is at ≈20°. c) PXRD patterns of $Li_3PS_{4-x}O_x$ ($x = 0$, 0.1, 0.25, 0.31, 0.5, and 1) from 25 to 33°. A shift to higher 2θ upon increasing O substitution confirms the successful incorporation of O into $Li_3PS_{4-x}O_x$. d) Energy-above-hull values calculated for $Li_3PS_{4-x}O_x$ ($x = 0.125$, 0.25, 0.3125, 0.5, and 1).

We report here the solid-state synthesis of glass–ceramic $Li_3PS_{4-x}O_x$ ($0 \leq x \leq 1$). Local structural environments in $Li_3PS_{4-x}O_x$ ($0 \leq x \leq 1$) are determined using solid-state nuclear magnetic resonance (NMR) spectroscopy, and variable-temperature electrochemical impedance spectroscopy (VT-EIS) is used to probe ion conduction. $Li_3PS_{3.69}O_{0.31}$ displays a significantly increased Li^+ conductivity, critical current density (CCD), and stability against Li metal while retaining its electrochemical stability window. $Li_3PS_{3.69}O_{0.31}$ in ASSB half-cells using TiS_2 cathode active material (CAM) delivers improved rate performance compared to Li_3PS_4. This work further illustrates the benefits of diversifying the anion sublattice to improve the performance of SEs.

2. Results and Discussion

2.1. Structure

$Li_3PS_{4-x}O_x$ ($x = 0$, 0.1, 0.25, 0.31, 0.5, and 1) compounds are synthesized using a solid-state synthesis approach (see Experimental Section). The parent compound, β-Li_3PS_4, belongs to the Pnma space group and is composed of PS_4^{3-} tetrahedral units with three distinct lithium sites, Li1, Li2, and Li3 (**Figure 1a**), which correspond to the 8d, 4b, and 4c Wyckoff positions, respectively.[12,39] Figure 1b shows the powder X-ray diffraction (PXRD) patterns of $Li_3PS_{4-x}O_x$ ($x = 0$, 0.1, 0.25, 0.31, 0.5, and 1) at 22 °C. No crystalline structure other than β-Li_3PS_4 is identified up to $x = 0.31$ in $Li_3PS_{4-x}O_x$. The slight shift in diffraction peaks to a larger 2θ upon increasing the value of x indicates the incorporation of O into the β-Li_3PS_4 structure (Figure 1c). Larger x ($x > 0.31$) in $Li_3PS_{4-x}O_x$ leads to a featureless powder diffraction pattern, making phase identification challenging. Such broadening of diffraction peaks in $Li_3PS_{4-x}O_x$ ($x > 0.31$) can be explained by the loss of crystallinity or internal strain induced by S→O substitution. The calculated energy above hull (E_{hull}) significantly increases beyond $x = 0.3125$ in $Li_3PS_{4-x}O_x$ (Figure 1d), suggesting an O-substitution limit ($x = 0.3125$) in $Li_3PS_{4-x}O_x$ without generating a substantial quantity of impurity phases.

Since the synthesized $Li_3PS_{4-x}O_x$ is a glass-ceramic material lacking long-range structural order, solid-state NMR is highly useful for investigating the local structure.[40] Therefore, further structural details of $Li_3PS_{4-x}O_x$ are obtained by analyzing the ^{31}P NMR, and the results are shown in **Figure 2a** and Figure S1a (Supporting Information). Peak analysis is performed on Li_3PS_4, $Li_3PS_{3.9}O_{0.1}$, $Li_3PS_{3.75}O_{0.25}$, and $Li_3PS_{3.69}O_{0.31}$. The corresponding quantitative results are shown in Figure S1b (Supporting Information) and Table S1 (Supporting Information). The most intense resonance at 86.3 ppm is assigned to the crystalline $(\beta\text{-}PS_4)^{3-}$,[39] in which the integral percentage decreases as the amount of O substitution increases to $x \geq 0.25$ (Figure S1b, Supporting Information). Upon O substitution, there is an increased linewidth of the β-PS_4^{3-} peak, suggesting structural disorder, which correlates well with the observed decreased crystallinity from the PXRD patterns (Figure 1a). The

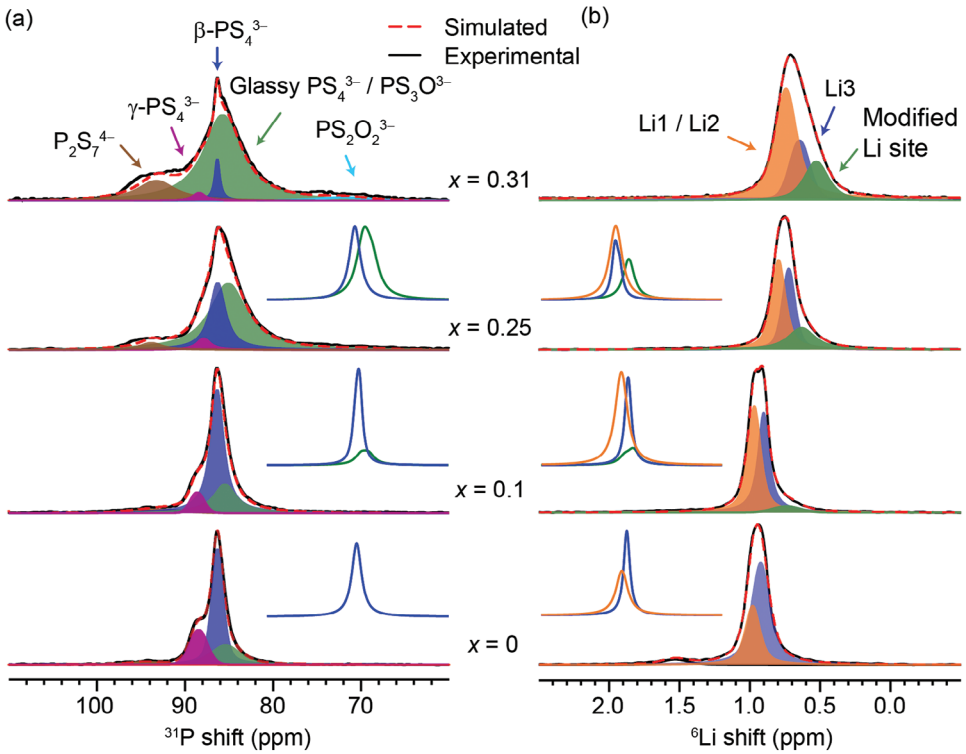

Figure 2. a) Experimental ^{31}P NMR spectra of $Li_3PS_{4-x}O_x$ ($x = 0$, 0.1, 0.25, 0.31). Quantitative results of components, including the phosphates at lower chemical shifts, are tabulated in Table S1 (Supporting Information). b) Experimental ^{6}Li spectra and deconvolution for $Li_3PS_{4-x}O_x$ ($x = 0$, 0.1, 0.25, 0.31). The quantitative results of components are tabulated in Table S2 (Supporting Information). The calculated ^{31}P and ^{6}Li NMR spectra of $Li_3PS_{4-x}O_x$ ($x =$ 0, 0.1, and 0.25) via DFT are shown as insets for comparison and confirm the peak assignments of the experimental ^{31}P and ^{6}Li spectra. Computational peak assignments are the same color as experimental assignments except for green computed peaks in ^{31}P, representing only PS_3O^{3-}. See Figure S3 and Table S3 (Supporting Information) for full details of the computed spectra.

^{31}P resonances at 88 and 93 ppm are assigned to the γ-$PS_4$3$^-$ unit and the $(P_2S_7)4^-$ unit, respectively.[30] The assignments for PS_4^{3-} and $P_2S_7^{4-}$ are also supported by the Raman spectra (Figure S2, Supporting Information). Upon O introduction beyond $x = 0.31$, lithium phosphate impurities are formed, evidenced via the ^{31}P resonances at 75, 70, 37, 9, and −3 ppm, assigned to $(PS_2O)^-$, $(PS_2O_2)^{3-}$, $(PSO_3)^{3-}$, $(PO_4)^{3-}$, and $(P_2O_7)^{4-}$, respectively (Figure S1a, Supporting Information).[13,22,24,30,41–44] Furthermore, a growing component at ≈85 ppm upon O substitution is assigned to a combined environment of glassy-$(PS_4)^{3-}$/$(PS_3O)^{3-}$, as their shifts are very close to each other, making accurate analysis challenging.[13,22,30] These results are also supported by E_{hull} (Figure 1d) and ΔH_{mix} calculations[12] suggesting low stability of $x = 0.5$ and 1, therefore, the thermodynamically favorable formation of phosphates.[12] Density functional theory (DFT) calculations for Li_3PS_4, $Li_3PS_{3.875}O_{0.125}$, and $Li_3PS_{3.75}O_{0.25}$ are carried out to simulate their ^{31}P NMR spectra (Figure 2a inset; Figure S3a, Supporting Information). Importantly, a new peak for the $(PS_3O)^{3-}$ unit is generated upon O introduction in Li_3PS_4. The close agreement in the relative chemical shift and intensity of the different phases between simulated and experimental spectra confirms successful O substitution and the spectral assignments.

To understand the evolution of the Li-local environments in $Li_3PS_{4-x}O_x$ with varying O substitution, we have employed ^{6}Li solid-state NMR (Figure 2b) and quantitative analysis, as shown in Figure S4 (Supporting Information) and Table S2 (Supporting Information). For Li_3PS_4, two peaks are assigned; one is the combined Li1/Li2 site corresponding to the 8d and 4b Wyckoff sites, respectively, and are assigned together due to their close distance and fast exchange.[39] The other is the Li3 site, which corresponds to the 4c Wyckoff site.[39] A small peak at 1.5 ppm is assigned to an unknown impurity, comprising 4.6% integral total. With increasing O substitution, the impurity decreases to a negligible amount. The broadening of the ^{6}Li resonance peaks for $Li_3PS_{3.69}O_{0.31}$ indicates reduced symmetry of the local Li^+ environments upon diversifying the anion sublattice.[5] In addition, the ^{6}Li integral percentage of the combined Li1/Li2 assignment increases to a maximum of 57.3% for $Li_3PS_{3.69}O_{0.31}$. A decrease in the ^{6}Li integral percentage of the Li3 site occurs upon O substitution from 64.7% to 20.4% for $Li_3PS_{3.69}O_{0.31}$ and the emergence of a modified Li site can be seen, comprising 22.3%. The Li^+ site diversification is also supported by computations and is reported to cause an increase in Li^+ conductivity via generating 3D pathways.[12] Furthermore, the ^{6}Li NMR shifts are computed for Li_3PS_4, $Li_3PS_{3.875}O_{0.125}$, and $Li_3PS_{3.75}O_{0.25}$ using the DFT optimized structures (Figure 2b inset; Figure S3b, Supporting Information). The results show good agreement with the experimental data in terms of peak intensity ratios and relative chemical shift for each assignment, which also supports successful experimental O substitution and validates the computational model.

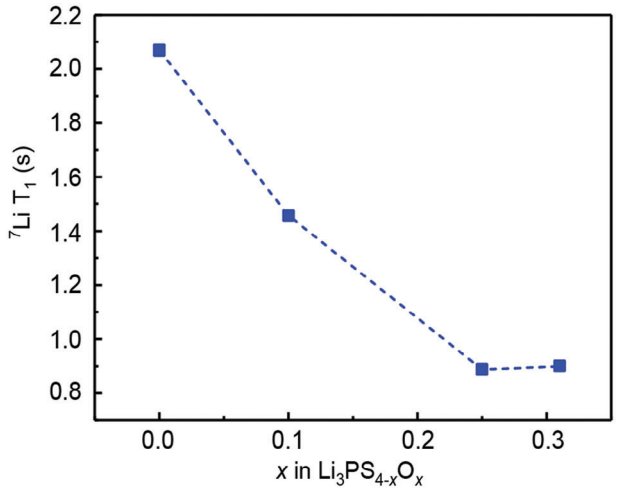

Figure 3. ^{7}Li NMR T_1 values for x in $Li_3PS_{4-x}O_x$ ($x = 0$, 0.1, and 0.31) at 22 °C.

2.2. Origin of Fast-Ion Conduction in $Li_3PS_{4-x}O_x$

To examine the change in Li^+ mobility for $Li_3PS_{4-x}O_x$ ($x = 0$, 0.1, 0.25, 0.31), ^{7}Li spin-lattice relaxation time (T_1) measurements w ere performed at 22 °C (**Figure 3** and Table S4, Supporting Information).[45] The decrease in T_1 upon O substitution indicates an increase in Li^+ mobility and may be attributed to PS_4^{3-}/PS_3O^{3-} coexistence in the anion sublattice.[11,46,47] The arrangement leads to a "frustrated" energy landscape and weakened Li^+ interactions.[9]

VT-EIS is performed to further examine the effect of O substitution on Li^+ transport. The conductivity isotherms, $\sigma'(\omega)$, of $Li_3PS_{4-x}O_x$ ($x = 0$, 0.1, 0.25, 0.31, 0.5, and 1) are shown in Figure S5 (Supporting Information) and that of $Li_3PS_{3.69}O_{0.31}$ is shown in **Figure 4a**. From the conductivity isotherms, the dependence of the real part of the complex conductivity, σ', on angular frequency, ω ($\omega = 2\pi f$; f = scanning frequency), can be approximated with the Jonscher-type power law, $\sigma' = \sigma_{DC} + A\omega^n$, where σ_{DC} is the DC ionic conductivity (frequency-independent conductivity), A is the alternating current coefficient, and n is the power law exponent.[48–50] From low (−40 °C) to high (120 °C) temperature, only one frequency-independent direct current (DC) plateau is observed (σ_{DC}), which represents long-range Li^+ transport and reflects bulk and grain boundary contributions.[48] One plateau, especially at a relatively low temperature (−40 °C), suggests that the macroscopic Li^+ conduction involves mainly the bulk process.[51] To further uncover any grain boundary contribution to the total long-range Li^+ resistance, as is often detrimental in oxide SEs,[48] the EIS spectra of $Li_3PS_{4-x}O_x$ ($x = 0$, 0.1, 0.25, 0.31, 0.5, and 1) at −40 °C were also fitted with an equivalent circuit of the type (RQ)Q; R represents resistor and Q represents constant phase element (Figure S6a, Supporting Information). One semicircle is detected in the Nyquist plots for $Li_3PS_{4-x}O_x$ at −40 °C (Figure S6, Supporting Information) with an exemplary Nyquist plot of $Li_3PS_{3.69}O_{0.31}$ at −40 °C shown in the inset of Figure 4a, indicating bulk and grain boundary resistances cannot be separated in this temperature range, as is typical due to the softness of sulfides,[48,52] and aligns well with the isotherm analysis. Analysis of the imaginary component of the complex electric modulus, M'' (see Supporting Information for discussion), as a function of ω (Figure S7, Supporting Information) indeed confirms that bulk processes are exclusively responsible for long-range Li^+ conduction. Negligible grain-boundary resistance within the oxysulfide $Li_3PS_{4-x}O_x$ ($x = 0$, 0.1, 0.25, 0.31, 0.5, and 1) is notable as other oxide SEs typically suffer from high grain-boundary resistance in addition to bulk resistance.[48]

The impact of x in $Li_3PS_{4-x}O_x$ on the long-range Li^+-migration activation energy barrier, $E_{a,DC}$, is determined using the following equation,[48,53,54]

$$\sigma_{DC}T = \sigma_0 \exp\left(-\frac{E_{a,DC}}{k_B T}\right) \quad (1)$$

where σ_0 represents the Arrhenius-type prefactor (see Supporting Information for in-depth discussion), k_B is the Boltzmann constant, and T is the absolute temperature. As illustrated in Figure 4b, a minimum $E_{a,DC}$ of 0.34 eV, is reached for $Li_3PS_{3.69}O_{0.31}$ among the series with $0 < x < 1$, indicating the optimal amount of O substitution to lower the energy barrier for macroscopic Li^+ conduction (Table S5, Supporting Information). The obtained $\sigma_{DC,25°C}$ of $Li_3PS_{3.69}O_{0.31}$ is 1.38 mS cm^{-1}, indicating a more than sevenfold enhancement in ionic conductivity compared to Li_3PS_4 ($\sigma_{DC,25°C} = 0.19$ mS cm^{-1}). Substituting O for S with $x > 0.31$ in $Li_3PS_{4-x}O_x$ leads to a reduction of σ_{DC} and an increase of $E_{a,DC}$ (Figure 4a–d). One reason for the trend is that many of the phosphates formed in $Li_3PS_{4-x}O_x$ compositions with $x > 0.31$ are poor Li^+ conductors, such as Li_3PO_4 (Figure S1, Supporting Information).[55]

To study how x in $Li_3PS_{4-x}O_x$ ($x = 0$, 0.1, 0.25, 0.31, 0.5, and 1) impacts Li^+ dynamics on different length scales and its effect on σ_{DC}, we examine the real part of complex resistivity at a fixed frequency, ρ' ($\rho' = M''/\omega$; see Supporting Information), as a function of temperature (T) (Figure S8, Supporting Information).[48] The activation barriers obtained from the Arrhenius-type fit for the high-T ($E_{a,\rho'HT}$) and low-T ($E_{a,\rho'LT}$) regime of ρ'-peaks are shown in Table S5 (Supporting Information). ρ'-peaks (1 MHz) of all $Li_3PS_{4-x}O_x$ ($x = 0$, 0.1, 0.25, 0.31, 0.5, and 1) compositions are collectively compared and summarized in Figure 4d. Since bulk processes are being probed here, $E_{a,\rho'HT}$ is comparable to $E_{a,DC}$ (i.e., long-range motion), while $E_{a,\rho'LT}$ represents the short-range motion.[48] Accordingly, $Li_3PS_{3.69}O_{0.31}$ exhibits the lowest energy barrier ($E_{a,\rho'HT}$), with a near minimum for $E_{a,\rho'LT}$. Moreover, the apex of the 1 MHz rate peak (Figure S8, Supporting Information) of $Li_3PS_{3.69}O_{0.31}$ appears at a lower temperature than that of other compositions. When more O is substituted into $Li_3PS_{4-x}O_x$, the rate peak shifts toward the side of high temperature, suggesting that ion motion is reduced.

The extracted prefactor (σ_0) shows a minimum for $Li_3PS_{3.69}O_{0.31}$ as in the case of the activation energies ($E_{a,\rho'HT}$ and $E_{a,DC}$). Furthermore, the maximum value of the crossover frequency, a rough approximation for jump frequency, is achieved for $Li_3PS_{3.69}O_{0.31}$, as shown in Figure S9 (see Supporting Information for an in-depth explanation). Thus, comparing the terms in the Arrhenius-type equation (Equation 1) and Arrhenius-type prefactor equation (Equation S1, Supporting Information), the effect of E_a dictates the trend of σ_{Li+} in $Li_3PS_{4-x}O_x$, while the modulation of prefactor does not follow the trend of σ_{Li+}

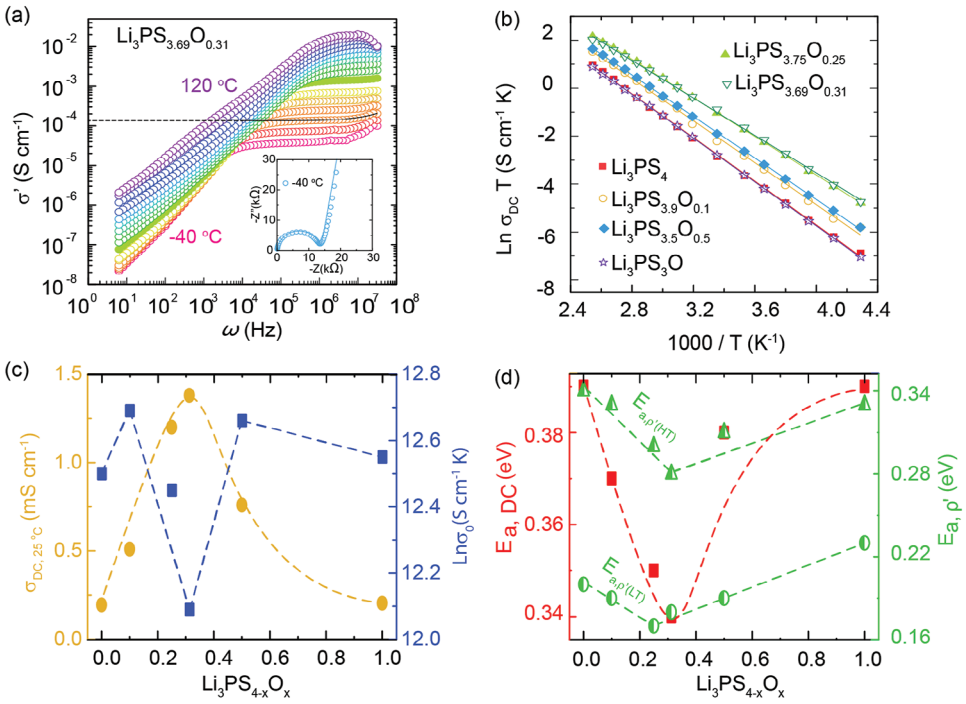

Figure 4. a) Conductivity isotherms from −40 to 120 °C, using $Li_3PS_{3.69}O_{0.31}$ as an example. The fitted line (using Jonscher-type power law, $\sigma' = \sigma_{DC} + A\omega^n$) is extrapolated to the *y*-axis to determine σ_{DC}. Filled green symbols represent the isotherm measured at 25 °C. Inset: Nyquist plot of $Li_3PS_{3.69}O_{0.31}$ at −40 °C. Equivalent circuit model details are documented in the Supporting Information (Figure S6 and Table S7, Supporting Information). b) Arrhenius plot for *x* in $Li_3PS_{4-x}O_x$ to extract $E_{a,DC}$. c) $\sigma_{DC,25°C}$ and σ_0, as determined from conductivity isotherm and Arrhenius plot analysis (d) $E_{a,DC}$, $E_{a,\rho'HT}$, and $E_{a,\rho'LT}$, as extracted from the Arrhenius plots of σ_{DC} and ρ'.

(see Supporting Information). According to the Meyer–Neldel rule,[56] the balance among prefactors and E_a leads to the highest Li^+ conduction for $Li_3PS_{3.69}O_{0.31}$.

To investigate the reported increase in dimensionality of Li^+ transport for *x* in $Li_3PS_{4-x}O_x$,[12,25] the Jonscher-type power law exponent, *n*, is analyzed (**Table 1**). *n* is an empirical indicator to describe the effective dimensions of ion conducting pathways, i.e., 1D, 2D, or 3D.[50,57] 3D correlated motion is typically associated with $n \geq 0.7$.[50,57] Through analyzing the conductivity isotherm (−20 °C) for $Li_3PS_{4-x}O_x$ ($x = 0$, 0.1, 0.25, 0.31, 0.5, and 1; Figure 4a; Figure S5, Supporting Information), a positive correlation between *n* and the amount of O is observed. This suggests a change in dimensionality of Li^+ motion from 2D (Li_3PS_4; $n = 0.62$) to 3D ($Li_3PS_{3.69}O_{0.31}$; $n = 0.87$). As further O substitution occurs, the value of *n* continues to increase, but the σ_{DC} decreases. This can be explained as local hopping in 3D, while the long-range Li^+ transport is compromised, as is also described from computations.[12] The physical process of this behavior is localized ion hopping without any macroscopic Li^+ conduction at higher O content.

With respect to Li^+ conductivity, the optimal amount of O is $x = 0.31$ in $Li_3PS_{4-x}O_x$. In parallel, the impact of O substitution on electronic conductivity, σ_{elec}, is evaluated for the pristine and optimized compositions using the DC polarization method.[38] The σ_{elec} of Li_3PS_4 (5.10×10^{-10} S cm^{-1}) is found to decrease upon O substitution to $Li_3PS_{3.69}O_{0.31}$ (3.29×10^{-10} S cm^{-1}; Figure S10, Supporting Information), which is desirable to minimize dendrite formation.[58]

Table 1. Summary of EIS analysis on $Li_3PS_{4-x}O_x$ ($x = 0$, 0.1, 0.25, 0.31, 0.5, and 1) for high-T activation energy barrier ($E_{a,\rho',HT}$), DC activation energy barrier ($E_{a,DC}$), DC ionic conductivity ($\sigma_{25\,°C}$), Arrhenius-type prefactor (σ_0), and the Jonscher-type power law exponent (*n*).

Sample	$E_{a,\rho',HT}$ [eV]	$E_{a,DC}$ [eV]	σ_{DC} [mS cm^{-1}]	Ln(σ_0) [S cm^{-1} K]	*n*
Li_3PS_4	0.34	0.39	0.19	12.50	0.62
$Li_3PS_{3.9}O_{0.1}$	0.33	0.38	0.51	12.69	0.65
$Li_3PS_{3.75}O_{0.25}$	0.30	0.35	1.20	12.45	0.85
$Li_3PS_{3.69}O_{0.31}$	0.28	0.34	1.38	12.09	0.87
$Li_3PS_{3.5}O_{0.5}$	0.31	0.37	0.76	12.66	0.88
Li_3PS_3O	0.33	0.39	0.20	12.55	0.95

2.3. Electrochemical Characterization of $Li_3PS_{4-x}O_x$ ($x = 0$ and 0.31)

Since improved ionic conductivity does not always indicate enhanced cell performance in ASSBs, it is important to perform other relevant electrochemical evaluations using $Li_3PS_{3.69}O_{0.31}$ as SE.[59] To better understand how O substitution impacts the CCD and stability against Li metal, Li|SE|Li symmetric cells were prepared. CCD is an important yet often overlooked parameter to determine the ability of SEs and SE-electrode interfaces to

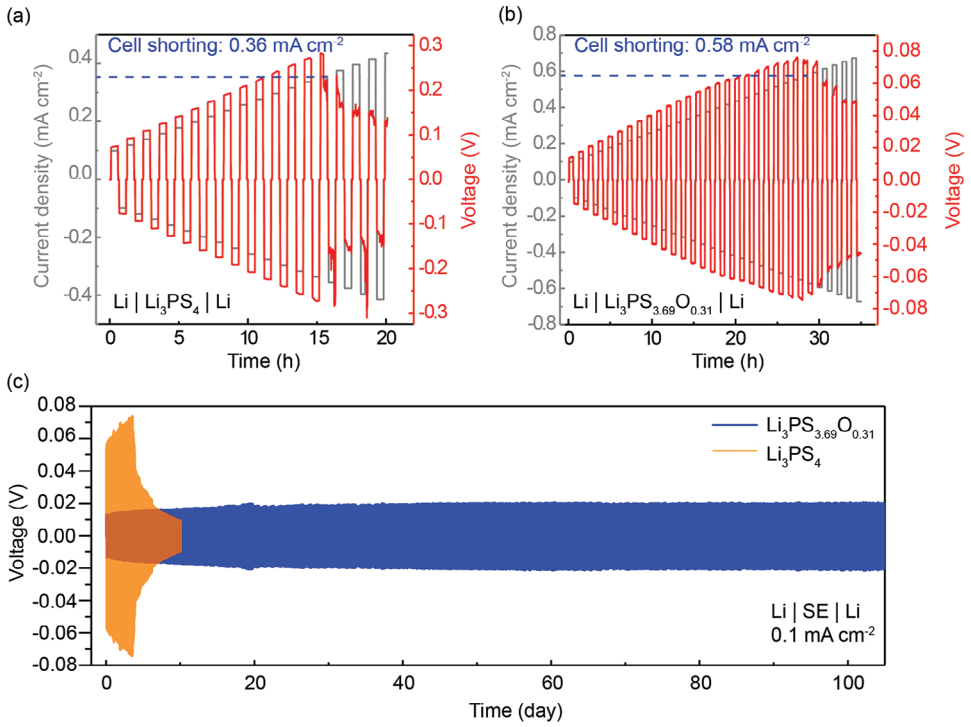

Figure 5. Comparison in electrochemical performance of $Li_3PS_{3.69}O_{0.31}$ and Li_3PS_4 in symmetric battery cells using Li metal foil as electrodes at 22 °C. a) The critical current density of Li_3PS_4, determined to be 0.36 mA cm^{-2}. b) The critical current density of $Li_3PS_{3.69}O_{0.31}$ determined to be 0.58 mA cm^{-2}. c) Long-term cycling performance of Li_3PS_4 and $Li_3PS_{3.69}O_{0.31}$ at 0.1 mA cm^{-2}.

suppress dendrite formation in ASSBs.[59] A high CCD is imperative for ASSBs with high-rate performance. By incrementally increasing the current density applied to the cell after each galvanostatic cycle, the room-temperature (22 °C) CCD is found at the point where the voltage shows a sharp decrease, indicating shorting of the cell due to Li dendrites, as shown in **Figure 5**a,b.[59] $Li_3PS_{3.69}O_{0.31}$ has a CCD of 0.58 mA cm^{-2} whereas Li_3PS_4 has a CCD of 0.36 mA cm^{-2} at room temperature. The improvement in CCD upon O substitution is likely due to the enhanced ionic conductivity, decreased electronic conductivity, and improved interfacial stability with Li metal.[59] The enhanced CCD suggests an improved ability of $Li_3PS_{3.69}O_{0.31}$ to be used in high-power density ASSBs in comparison to Li_3PS_4.[59] Furthermore, $Li_3PS_{3.69}O_{0.31}$ shows a significant improvement in long-term symmetric cycling stability at 0.1 mA cm^{-2} against Li metal than Li_3PS_4 as shown in Figure 5c. Li_3PS_4 experiences cell shorting after ≈6 days at room temperature while $Li_3PS_{3.69}O_{0.31}$ can cycle over 100 days without cell shorting. The small increase in voltage over time indicates a minimal increase in interfacial resistance between the Li metal electrode and $Li_3PS_{3.69}O_{0.31}$, in comparison to that with Li_3PS_4 (Figure 5c)–further suggesting that $Li_3PS_{3.69}O_{0.31}$ shows greater interfacial stability against Li metal than Li_3PS_4.[13] Computations report that the chemical and electrochemical reactivity of LPS and LPSO with Li metal are similar and suggest that small amounts of Li_3PO_4 can be formed at Li-metal|$Li_3PS_{3.69}O_{0.31}$ interfaces and potentially provide stabilization against Li metal.[12] Importantly, the ionic conductivity of the likely disordered and defect-containing Li_3PO_4 SEI is not expected to be a limiting factor.[12]

To assess the electrochemical stability window of Li_3PS_4 (LPS) and $Li_3PS_{3.69}O_{0.31}$ (LPSO) and the capacity generated from using them as a pseudo-active material, cells were assembled using a Li–In anode, SE separator, and a 3SE:C (mass ratio) composite cathode, as is commonly reported in the literature.[35–37,60–62] The use of carbon, in this case Super P, increases the electronic conductivity and allows for degradation current to be more accurately measured than without the use of carbon.[35,60,61]

According to computations, the intrinsic stability window (voltage range with no Li^+ loss or uptake; i.e., the voltage range where the SE does not de/lithiate) of LPS (1.11 V–1.77 V vs Li–In) should not change upon O substitution.[12] Below 1.11 V versus Li–In, LPS forms Li_2S + P and LPSO forms Li_2S + Li_3PO_4 + P; above 1.77 V versus Li–In, LPS forms S + P_2S_5 and LPSO forms S + Li_3PO_4 + P_2S_5.[12] The reversible redox (de/lithiate) activity of LPS, as well as its subsequent redox products, has been reported and shown to be complex. However, the effective electrochemical stability window of the SE can be experimentally estimated.[11,34,35,38,63,64]

The cyclic voltammograms of cycle 1 for LPS and LPSO carbon composite cells are shown in **Figure 6**a, and the corresponding capacity from the galvanostatically cycled cells over 40 cycles is shown in Figure 6b with the voltage profiles shown in Figure 6c,d. Cyclic voltammetry (CV) indicates retention of the stability window based on the nearly overlapped voltammograms of LPS/C and LPSO/C composites. Notably, the experimental upper stability limit of the SE oxidation/delithiation for both SEs is ≈2.25 V versus Li–In, which is higher than the computed

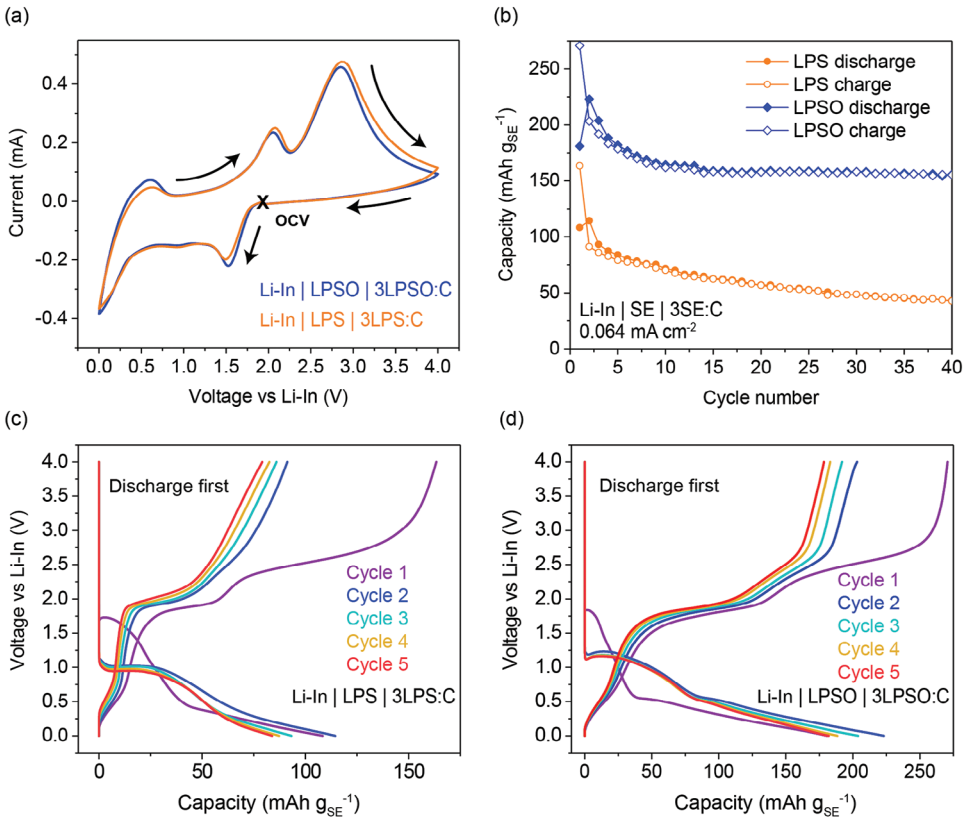

Figure 6. a) Cyclic voltammograms of LPS and LPSO with a scan rate of 0.2 mV s^{-1}. See Figure S11 (Supporting Information) for voltammograms of subsequent cycles 2 and 3. b) Room-temperature capacity versus cycle number. All galvanostatic cycling is performed using a current density of 0.064 mA cm^{-2}. c) Voltage profiles of cycles 1–5 for Li–In|Li_3PS_4|3Li_3PS_4:C. d) Voltage profiles of cycles 1–5 for Li–In|$Li_3PS_{3.69}O_{0.31}$|3$Li_3PS_{3.69}O_{0.31}$:C.

intrinsic value (1.77 V vs Li–In), as is common in literature[11,26,35,38] A cathodic peak starting at ≈1.9 V versus Li–In likely corresponds to $S_y \rightarrow S_y^{2-}$ (e.g., Li_2S generation) from small amounts of elemental sulfur impurities present from the synthesis, based on the onset voltage.[35,38,60] After cycle 1, the peak is no longer observed in CV, or as a capacity plateau from galvanostatic cycling (Figure 6c,d), as the sulfur impurities are likely consumed by other redox reactions and indicates that elemental sulfur → Li_2S is not part of the reversible capacity generated.[11] A small cathodic peak beginning at ≈1.10 V versus Li–In is assigned to the onset of the partially reversible SE lithiation/reduction,[12] which generates significant capacity starting from the 2nd cycle when galvanostatically cycled (Figure 6b–d), indicating enhanced SE lithiation/reduction upon prior PS_4^{3-} oxidation (SE delithiation).[11] The cathodic peak at <0.6 V versus Li–In is from the reduction (lithiation) of the redox product, P, toward Li_3P (includes Li_2O + Li_3P generation from Li_3PO_4 reduction in the LPSO cell at <0.1 V vs Li–In), as is reported to be the phase equilibria with Li metal for Li_3PS_4 and $Li_3PS_{3.75}O_{0.25}$.[12,37,38] The first anodic scan shows at ≈0.5 V versus Li–In and is assigned to the oxidation of the carbon. A large peak centered at ≈2.1 V versus Li–In is[35] tentatively assigned to a conversion reaction of Li_2S and Li_3P to form lithium thiophosphate glasses (including thiophosphate polyhedra), based on reports of other thiophosphate SEs[36,38] and is highly reversible based on the stable cycling performance and capacity plateau at that voltage (Figure 6c,d).[35] Upon subsequent cycles, a passivation layer is formed for both SEs that impedes further SE oxidation (Figure S11, Supporting Information). The retention of the effective electrochemical stability window after O substitution supports computational findings that the optimal amount of O in $Li_3PS_{4-x}O_x$ will retain the intrinsic electrochemical stability window of LPS.[12]

As expected from the literature, significant capacity is generated from the SE and subsequent redox products, which can be advantageously leveraged if it occurs in the same voltage window as ASSB operation and is reversible.[34,36,37,60,63] Galvanostatic cycling of the carbon-composite LPS cells shows a lower 1st discharge capacity of 108 mAh g_{SE}^{-1} and 1st charge capacity of 163 mAh g_{SE}^{-1} compared to 181 mAh g_{SE}^{-1} and 271 mAh g_{SE}^{-1} for LPSO. The increase in ionic conductivity likely allows a greater amount of capacity-generating redox reactions to occur due to improved reaction kinetics. This suggests improvements in ASSB capacity when using LPSO as the SE in comparison to LPS. The second discharge for both LPS and LPSO show an increase in capacity to 114 and 223 mAh g_{SE}^{-1}, respectively. The increase in capacity is likely due to the redox activity of the redox products formed during Cycle 1.[36] On the 2nd charge, the capacity plateaus corresponding to PS_4^{3-} oxidation are decreased due to the passivation interphase formed and accordingly, the capacity decreases to 91 mAh g_{SE}^{-1} for LPS and 203 mAh g_{SE}^{-1} for LPSO. Ortho-thiophosphate oxidation to

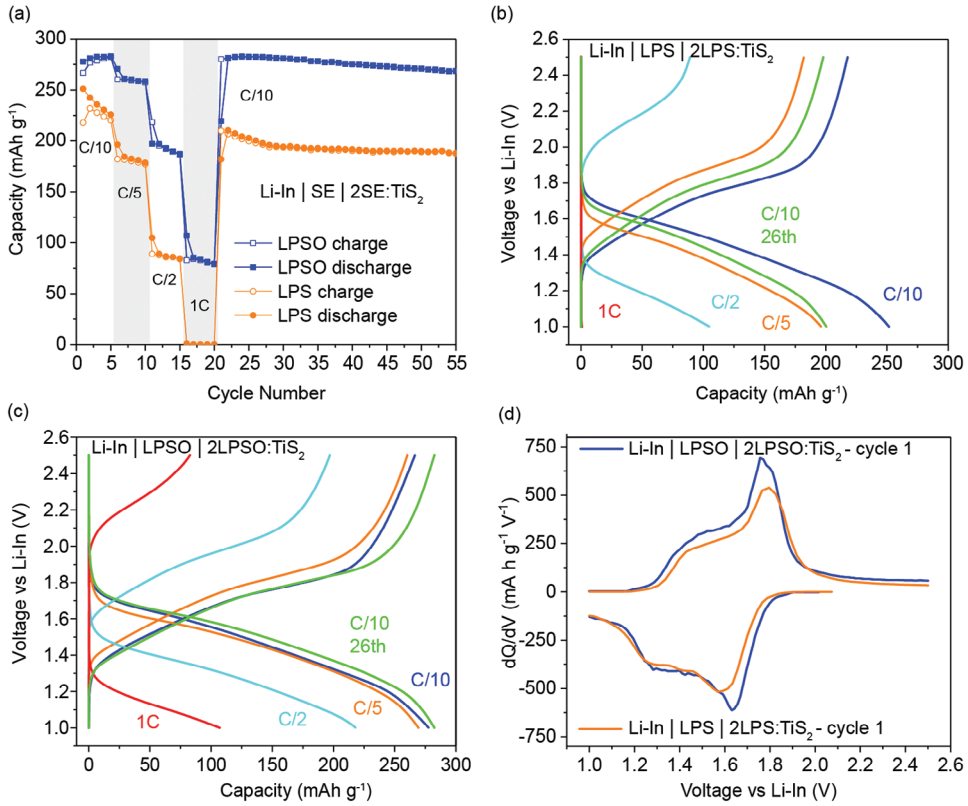

Figure 7. Galvanostatic cycling of Li–In|SE|2SE:TiS_2 (SE = Li_3PS_4 or $Li_3PS_{3.69}O_{0.31}$) half-cells at 0.1, 0.2, 0.5, and 1 C. a) Capacity versus cycle number. b) Voltage profiles of the first cycle at each C-rate for the half-cell containing Li_3PS_4. c) Voltage profiles of the first cycle at each C-rate for half-cell containing $Li_3PS_{3.69}O_{0.31}$. d) dQ/dV versus voltage of Cycle 1 for 2LPS:TiS_2 and 2LPSO:TiS_2 containing half-cells.

pyro/meta-thiophosphates is reported to be partially reversible during lithiation due to the complex and coupled redox chemistry of thiophosphates,[35,64] requiring a sulfide or polysulfide species for stoichiometric balance.[65] From Figure 6b, it can be seen that LPS carbon composite cells have nearly half the capacity generated compared with LPSO carbon-composite cells after 40 cycles. This suggests that the composition and transport properties of the redox interphases formed against the C are improved for LPSO, potentially due to the improved Li^+ conductivity and stability of the LPSO separator.[35] Although, we note the voltage window used here is wider than that in typical ASSBs (≈1–4 V vs Li–In), and redox of the decomposition products, particularly at low voltage, is contributing to some of the capacity in both carbon-composite cells. Despite this, improvements in the reversible capacity of LPSO and its redox products against C as well as retention of the electrochemical stability window further display the improvements of LPS via O substitution.

To further examine the performance of LPSO in ASSBs, half-cells were assembled using TiS_2 as the CAM and Li–In alloy as the anode. The corresponding Nyquist plots and equivalent circuit models at 22 °C are shown in Figure S12 (Supporting Information). The LPS and LPSO containing half-cells have a CAM/SE resistance of 131 and 200 Ω, respectively. The larger CAM/SE resistance of the LPSO-containing half-cell before cycling is expected for oxide-containing materials due to their relatively low wettability. However, due to the stability of oxides versus sulfides, this interfacial resistance does not increase significantly with cycling for CAM/LPSO (247 Ω after 55 cycles), while impurities generated from parasitic reactions in CAM/LPS further increase the 131 Ω to a higher value of 852 Ω (Figure S12, Supporting Information). The galvanostatic rate performance was determined at 0.1, 0.2, 0.5, and 1 C for five cycles each, then at 0.1 C for 35 cycles using 239 mAh g^{-1} as the theoretical capacity for TiS_2 (**Figure 7a**). The corresponding voltage profiles for the first cycle of each C-rate, as well as the 26th cycle, are shown in Figure 7b,c. The first discharge (278 mAh g^{-1}) and first charge (267 mAh g^{-1}) capacity for the Li–In|LPSO|TiS_2:2LPSO half-cell is greater than that of Li–In|LPS|TiS_2:2LPS (218 mAh g^{-1} charge and 251 mAh g^{-1} discharge capacity). Notably, the capacity for both half-cells is greater than the theoretical capacity of TiS_2 (239 mAh g^{-1}), which is likely due to the SE redox,[11,35,66] as discussed above, and potentially from redox of unknown phases from reactions of the SE and TiS_2, as has been suggested in the literature of similar sulfide catholytes.[67] The SE 10 h high-energy ball milling process and 5 h planetary milling of TiS_2 may play a role in the surface layer of the particles to more readily react/decompose. The improvement in total capacity for the LPSO half-cell is likely due to a combination of several reasons: 1) the higher ionic conductivity and stability against Li metal of LPSO in the separator, 2) better utilization of the CAM capacity in the catholyte via improved Li^+ percolation kinetics,[68] 3) the increased capacity of its redox products compared to that of LPS (Figure 6b). After the first cycle, the LPS cell shows a trend of decreasing capacity, whereas using LPSO shows capacity retention. The ASSB half-cell using LPSO shows a small

amount of extra capacity by the fifth cycle and even after 26 cycles with a discharge–charge capacity of ≈282 mAh g^{-1}, respectively, potentially due to the formation of a stable Li–In/LPSO and/or TiS_2/LPSO interface. Furthermore, when cycled at 1 C, cells containing LPS have a discharge and charge capacity of ≈0 mAh g^{-1} (Figure 7a,b), in contrast to LPSO with a capacity of ≈80 mAh g^{-1}–indicating the enhanced rate performance of ASSBs using LPSO over LPS. The improved capacity at a higher C-rate is likely due to the enhanced ionic conductivity of LPSO in the separator and catholyte. The differential capacity (dQ/dV) plot of Cycle 1 is shown in Figure 7d and illustrates the typical redox peaks for $Ti^{3+/4+}$ for both LPS- and LPSO-containing cells.[11,67,69] A small amount of dQ/dV is observed at low and high voltage for LPS- and LPSO-containing cells, which may be due to the redox of the SE decomposition products as described above and/or redox-active interphase that is formed between SE and TiS_2 upon mixing–contributing to the extra capacity.[67] dQ/dV plots of Cycles 1, 2, and 26 are shown in Figure S13 (Supporting Information). At Cycle 26, the reduction in capacity is also reflected in the loss in intensity of the dQ/dV peak in the LPS-containing cell in comparison to the LPSO-containing cell.

3. Conclusion

In summary, we have synthesized new oxysulfides, specifically $Li_3PS_{4-x}O_x$ ($0 < x \leq 1$), with $Li_3PS_{3.69}O_{0.31}$ exhibiting the best performance with respect to σ_{DC} (1.38 mS cm^{-1}) and $E_{a,DC}$ (0.34 eV). PS_3O^{3-} units are generated upon O substitution, resulting in a diversified anion sublattice that induces a frustrated and flattened energy landscape. The reduction in the activation barrier plays a dominant role over the Arrhenius prefactor in enhancing σ_{DC} for this material class. Moreover, we also observe a change from 2D to 3D Li^+ transport in $Li_3PS_{4-x}O_x$. As substituted O surpasses the optimal amount ($x = 0.31$), interruption of long-range diffusion combined with the generation of low-conducting phosphates, such as Li_3PO_4, degrades the σ_{DC}. Optimal O substitution improves the CCD, enhances stability against Li metal anodes, and maintains the effective electrochemical stability window. Furthermore, $Li_3PS_{3.69}O_{0.31}$ delivers increased gravimetric capacity and improved rate performance upon cycling in ASSBs using TiS_2 as the active cathode.

4. Experimental Section

Synthesis of $Li_3PS_{4-x}O_x$ ($x = 0, 0.1, 0.25, 0.31, 0.5,$ and 1): Stoichiometric amounts of Li_2S (Alfa Aesar, 99.9%), P_2S_5 (Sigma–Aldrich, 99.9%), and P_2O_5 (Alfa Aesar, 99.99%) were mixed using Agar mortar and pestle for 10 min and then homogenized for 10 h under vacuum using a SPEX 8000 M high-energy mixer. The ratio of the milling media (two zirconia balls; diameter = 10 mm) mass to the total mass of precursors was ≈14:1. The mixed powders were pressed into a 6-mm diameter pellet (Across International) under a pressure of ≈400 MPa and then heated at 230 °C for 2 h (ramping rate of 1 C min^{-1}) followed by natural cooling. The approximate pellet density used was 1.8 g cm^{-3}. Sample handling and heat treatment were all performed under Ar (H_2O < 1 ppm and O_2 < 1 ppm) in a glovebox (MBraun).

Materials Characterization: Powder X-ray diffraction measurements were conducted with a PANalytical X'Pert Pro-MPD Powder Diffractometer with Cu-Kα radiation. Kapton film was employed to reduce reactions of $Li_3PS_{4-x}O_x$ with moist air. Magic-angle-spinning (MAS) NMR measurements on $Li_3PS_{4-x}O_x$ ($x = 0, 0.1, 0.25, 0.31, 0.5,$ and 1) were performed on a Bruker Avance III 500 MHz NMR spectrometer with a spinning rate of 25 kHz at room temperature. ^{31}P (Larmor frequency = 202.404 MHz) NMR spectra were acquired using a Hahn Echo pulse sequence with a pulse length of 4.2 µs and a recycle delay of 200 s. A single pulse with a pulse length of 4.750 µs was employed to obtain ^{6}Li (Larmor frequency = 73.58 MHz) NMR spectra using a recycle delay of 200 s. $^{6,7}Li$ and ^{31}P chemical shifts were referenced to solid LiCl (−1.1 ppm) and 85% H_3PO_4 (0 ppm), respectively. Inversion recovery pulse sequence was used to measure ^{7}Li T_1.

Structural Relaxations and Energy Calculations: For energy above hull calculations, a series of LPSO structures were randomly generated with Pymatgen and ordered based on Coulomb interactions to determine 25 structures with the lowest energies. Those structures were then relaxed at the DFT level and their total energies were calculated. Comparing the total energy to the energies of decomposed products (Li_3PS_4 and Li_3PO_4) generated the energy above hull.

Structural relaxations and energetics were performed according to the literature.[12] DFT calculations were done using the projector-augmented-wave method[70,71] with Perdew–Burke–Ernzerhof generalized-gradient approximation (PBE-GGA)[72] and dispersion corrected optB88[73,74] functional, as implemented in the VASP package.[71,70] In alignment with the settings used in the Materials Project database calculations, a plane-wave cut-off of 520 eV is used for initial structural relaxations.[75] Reciprocal space discretization of 25 k-points $Å^{-1}$ was used for DFT relaxations, with convergence criteria set as 10^{-6} eV in total energy for electronic steps and 0.02 eV $Å^{-1}$ in interatomic forces for ionic relaxations. Pymatgen and Pymatgen-diffusion packages were utilized to generate the input file and post-processing analysis.[76] The pre-relaxed structures of β-Li_3PS_4, *Pnma* (mp-985583) and γ-Li_3PS_4, *Pmn*2_1 (ICSD# 180318) were extracted from the Materials Project (MP) database[77,78] and ICSD,[79] respectively. $Li_3PS_{4-x}O_x$ structures were generated using isovalent substitution with O^{2-} on the S^{2-} sites.[12] All symmetrically distinct S–O orderings are determined to identify the structure with the lowest energy through DFT calculations.

NMR Computations: The isotropic chemical shifts are calculated by magnetic shielding using perturbation theory (linear response) as implemented in VASP[80,81] while DFT energy calculations were done with PBE/PAW approach.[72] All the parameters involved were the same as default settings in Pymatgen. The calibration factors of $^{6/7}Li$ (+90.5 ppm) and ^{31}P (+254 ppm) were estimated from the difference between experimental and computed isoshift of pristine β-Li_3PS_4. All the configurations that were selected for NMR calculations were carried out on the lowest total energy among all the DFT-optimized structures of the same O doping level. An energy cutoff of 600 eV was applied to the system to meet the high-accuracy criterion for such calculations. For better visualization, Lorentzian line-broadening is conducted with broadening factors listed in Table S3 (Supporting Information).

Impedance Measurements: Impedance measurements on $Li_3PS_{4-x}O_x$ ($x = 0, 0.1, 0.25, 0.31, 0.5,$ and 1) were carried out using a Gamry Ref 600+ and in-house built PEEK cylindrical cell[82] with indium foil (3/16 in diameter) as blocking electrodes. Variable-temperature Nyquist spectra were collected from −40 to 120 °C (increment of 10 °C per measurement, except 25 °C) within a scanning frequency range from 5 MHz to 0.1 Hz under a biased potential of 100 mV. All the measurements were performed in a Cincinnati Sub-Zero Temperature Chamber under dry air atmosphere to prevent H_2O contamination.

DC Polarization: Electronic conductivity measurements were performed using the DC polarization method[38] using in-house built split cells (diameter = 10 mm) using PEEK insulating outer and stainless-steel plungers as current collectors and ion-blocking electrodes.

Symmetric cycling: Symmetric cycling was performed using the split cells for CCD and long-term cycling. 120 mg of SE was pressed at 300 MPa and then a piece of 0.1 mm thick Li foil (1/4 in diameter) was applied to both sides of the SE pellet and cycled under 5 MPa stack pressure[83] using 30 min current in each direction with 5 min rest in between changing current directions. For CCD, the current density is stepped up after each successive cycle until cell shorting began.

ASSB Assembly: All-solid-state-battery half-cells were prepared using the in-house built 10 mm split cells with stainless-steel plungers as current collectors. For 3SE:carbon half-cells, first, 100 mg of SE was pressed in the split cells at 300 MPa for 10 s and then ≈12 mg of the hand-mixed composite (carbon is Super P) was carefully spread onto one side of the pellet and pressed at 300 MPa for 10 s. On the other side of the pellet, a piece of In foil (5/16 in diameter) weighing ≈ 32 mg was placed onto the pellet followed by Li foil (3/16 in diameter) weighing ≈1 mg. The cell was sealed using vacuum grease and then cycled under ≈30 MPa stack pressure at 22 °C. For cyclic voltammetry measurements, a scan rate of 0.2 mV s^{-1} was used between 0 and 4 V versus Li–In. For galvanostatic measurements, a current density of 0.064 mA cm^{-2} was used and cycled between 0 and 4 V versus Li–In.

For TiS_2:2SE half-cells, TiS_2 (Sigma, 99.9%) was planetary milled for 5 h at 300 RPM to decrease particle size[84] and then hand-milled with Li_3PS_4 or $Li_3PS_{3.69}O_{0.31}$ in a 1:2 (TiS_2:SE) mass ratio using pestle and mortar for 10 min. No carbon additive was used due to the high electronic conductivity of TiS_2.[67,84] 100 mg of SE was pressed at 300 MPa for 10 s then ≈12 mg of catholyte was spread on one side of the pellet, corresponding to an areal loading of ≈1.25 mAh cm^{-2}, and pressed at 300 MPa for 10 s. On the other side of the pellet, a piece of In foil (5/16 in diameter) weighing ≈32 mg was then placed onto the pellet followed by Li foil (3/16 in diameter) weighing ≈1 mg. The cell was sealed using vacuum grease and then cycled under ≈30 MPa stack pressure at room temperature between 1 and 2.5 V versus Li–In.

Supporting Information

Supporting Information is available from the Wiley Online Library or from the author.

Acknowledgements

The authors acknowledge the support from the National Science Foundation under grant no. DMR-1847038 and from the NSF MRSEC program (NSF DMR-1720139). All solid-state NMR experiments were performed at the National High Magnetic Field Laboratory, which is supported by National Science Foundation Cooperative Agreement Nos. DMR-1644779 and DMR-2128556 and the State of Florida. The authors want to thank William Stoffel for helping to design and fabricate the in-house split-cells.

Conflict of Interest

The authors declare no conflict of interest.

Data Availability Statement

The data that support the findings of this study are available from the corresponding author upon reasonable request.

Keywords

energy storage, ionic conductivity, solid electrolytes, solid-state NMR

Received: August 22, 2023
Revised: October 28, 2023
Published online: December 6, 2023

[1] J. Janek, W. G. Zeier, *Nat. Energy* **2016**, *1*, 16141.
[2] T. Famprikis, P. Canepa, J. A. Dawson, M. S. Islam, C. Masquelier, *Nat. Mater.* **2019**, *18*, 1278.
[3] T. Placke, R. Kloepsch, S. Dühnen, M. Winter, *J. Solid State Electrochem.* **2017**, *21*, 1939.
[4] Y. Kato, S. Hori, T. Saito, K. Suzuki, M. Hirayama, A. Mitsui, M. Yonemura, H. Iba, R. Kanno, *Nat. Energy* **2016**, *1*, 16030.
[5] S. V. Patel, S. Banerjee, H. Liu, P. Wang, P.-H. Chien, X. Feng, J. Liu, S. P. Ong, Y. Y. Hu, *Chem. Mater.* **2021**, *33*, 1435.
[6] M. J. Deck, Y. Y. Hu, *J. Mater. Res.* **2023**, *38*, 2631.
[7] Y. Zeng, B. Ouyang, J. Liu, Y. W. Byeon, Z. Cai, L. J. Miara, Y. Wang, G. Ceder, *Science* **2022**, *378*, 1320.
[8] B. C. Wood, J. B. Varley, K. E. Kweon, P. Shea, A. T. Hall, A. Grieder, M. Ward, V. P. Aguirre, D. Rigling, E. Lopez Ventura, C. Stancill, N. Adelstein, *Philos. Trans. R. Soc. A Math. Phys. Eng. Sci.* **2021**, *379*, 20190467.
[9] D. Di Stefano, A. Miglio, K. Robeyns, Y. Filinchuk, M. Lechartier, A. Senyshyn, H. Ishida, S. Spannenberger, D. Prutsch, S. Lunghammer, D. Rettenwander, M. Wilkening, B. Roling, Y. Kato, G. Hautier, *Chem* **2019**, *5*, 2450.
[10] M. Botros, J. Janek, *Science* **2022**, *378*, 1273.
[11] T. P. Poudel, M. J. Deck, P. Wang, Y. Y. Hu, *Adv. Funct. Mater.* **2023**, 2309656.
[12] S. Banerjee, M. L. Holekevi Chandrappa, S. P. Ong, *ACS Appl. Energy Mater.* **2022**, *5*, 35.
[13] X. Chi, Y. Zhang, F. Hao, S. Kmiec, H. Dong, R. Xu, K. Zhao, Q. Ai, T. Terlier, L. Wang, L. Zhao, L. Guo, J. Lou, H. L. Xin, S. W. Martin, Y. Yao, *Nat. Commun.* **2022**, *13*, 2854.
[14] K. Takada, M. Osada, N. Ohta, T. Inada, A. Kajiyama, H. Sasaki, S. Kondo, M. Watanabe, T. Sasaki, *Solid State Ion.* **2005**, *176*, 2355.
[15] M. Lazar, S. Kmiec, A. Joyce, S. W. Martin, *ACS Appl. Energy Mater.* **2020**, *3*, 11559.
[16] T. Ohtomo, A. Hayashi, M. Tatsumisago, K. Kawamoto, *J. Non. Cryst. Solids* **2013**, *364*, 57.
[17] S. Banerjee, X. Zhang, L. W. Wang, *Chem. Mater.* **2019**, *31*, 7265.
[18] Y. Tao, S. Chen, D. Liu, G. Peng, X. Yao, X. Xu, *J. Electrochem. Soc.* **2015**, *163*, A96.
[19] M. Cengiz, H. Oh, S.-H. Lee, *J. Electrochem. Soc.* **2019**, *166*, A3997.
[20] K. Suzuki, M. Sakuma, S. Hori, T. Nakazawa, M. Nagao, M. Yonemura, M. Hirayama, R. Kanno, *Solid State Ionics* **2016**, *288*, 229.
[21] Z. Sun, Y. Lai, N. Lv, Y. Hu, B. Li, L. Jiang, J. Wang, S. Yin, K. Li, F. Liu, *ACS Appl. Mater. Interfaces* **2021**, *13*, 54924.
[22] M. Tatsumisago, H. Yamashita, A. Hayashi, H. Morimoto, T. Minami, *J. Non. Cryst. Solids* **2000**, *274*, 30.
[23] Y. Sun, K. Suzuki, K. Hara, S. Hori, T. A. Yano, M. Hara, M. Hirayama, R. Kanno, *J. Power Sources* **2016**, *324*, 798.
[24] K. H. Kim, S. W. Martin, *Chem. Mater.* **2019**, *31*, 3984.
[25] X. Wang, R. Xiao, H. Li, L. Chen, *Phys. Chem. Chem. Phys.* **2016**, *18*, 21269.
[26] Y. Zhu, X. He, Y. Mo, *ACS Appl. Mater. Interfaces* **2015**, *7*, 23685.
[27] Y. Zhu, X. He, Y. Mo, *Adv. Sci.* **2017**, *4*, 1600517.
[28] K. Homma, M. Yonemura, T. Kobayashi, M. Nagao, M. Hirayama, R. Kanno, *Solid State Ionics* **2011**, *182*, 53.
[29] M. Tachez, J. Malugani, R. Mercier, G. Robert, *Solid State Ionics* **1984**, *14*, 181.
[30] M. Gobet, S. Greenbaum, G. Sahu, C. Liang, *Chem. Mater.* **2014**, *26*, 3558.
[31] Z. Liu, W. Fu, E. A. Payzant, X. Yu, Z. Wu, N. J. Dudney, J. Kiggans, K. Hong, A. J. Rondinone, C. Liang, *J. Am. Chem. Soc.* **2013**, *135*, 975.
[32] N. J. J. De Klerk, E. Van Der Maas, M. Wagemaker, *ACS Appl. Energy Mater.* **2018**, *1*, 3230.
[33] R. Xiao, H. Li, L. Chen, *Sci. Rep.* **2015**, *5*, 14227.
[34] T. Hakari, M. Nagao, A. Hayashi, M. Tatsumisago, *J. Power Sources* **2015**, *293*, 721.

[35] G. F. Dewald, S. Ohno, M. A. Kraft, R. Koerver, P. Till, N. M. Vargas-Barbosa, J. Janek, W. G. Zeier, *Chem. Mater.* **2019**, *31*, 8328.
[36] D. H. S. Tan, E. A. Wu, H. Nguyen, Z. Chen, M. A. T. Marple, J. M. Doux, X. Wang, H. Yang, A. Banerjee, Y. S. Meng, *ACS Energy Lett* **2019**, *4*, 2418.
[37] T. K. Schwietert, V. A. Arszelewska, C. Wang, C. Yu, A. Vasileiadis, N. J. J. De Klerk, J. Hageman, T. Hupfer, I. Kerkamm, Y. Xu, E. Van Der Maas, E. M. Kelder, S. Ganapathy, M. Wagemaker, *Nat. Mater.* **2020**, *19*, 428.
[38] S. Ohno, C. Rosenbach, G. F. Dewald, J. Janek, W. G. Zeier, *Adv. Funct. Mater.* **2021**, *31*, 2010620.
[39] H. Stöffler, T. Zinkevich, M. Yavuz, A. Senyshyn, J. Kulisch, P. Hartmann, T. Adermann, S. Randau, F. H. Richter, J. Janek, S. Indris, H. Ehrenberg, *J. Phys. Chem. C* **2018**, *122*, 15954.
[40] X. Li, M. Deck, Y. Y. Hu, in *Transition Metal Oxides for Electrochemical Energy Storage*, (Eds: J. Nanda, V. Augustyn),VCH, Weinheim, Germany **2022**, pp 299–318.
[41] K. Hirai, M. Tatsumisago, M. Takahashi, T. Minami, *J. Am. Ceram. Soc.* **1996**, *79*, 349.
[42] F. Mizuno, T. Ohtomo, A. Hayashi, K. Tadanaga, T. Minami, M. Tatsumisago, *J. Ceram. Soc. Japan, Suppl.* **2004**, *112*, S709.
[43] T. Ohtomo, F. Mizuno, A. Hayashi, K. Tadanaga, M. Tatsumisago, *J. Power Sources* **2005**, *146*, 715.
[44] S. Kmiec, A. Joyce, D. Bayko, S. W. Martin, *J. Non. Cryst. Solids* **2020**, *534*, 119776.
[45] N. Bloembergen, E. M. Purcell, R. V. Pound, *Phys. Rev.* **1948**, *73*, 679.
[46] J. Popovic, D. Brandell, S. Ohno, K. B. Hatzell, J. Zheng, Y. Y. Hu, *J. Mater. Chem. A* **2021**, *9*, 6050.
[47] N. Wu, P.-H. Chien, Y. Qian, Y. Li, H. Xu, N. S. Grundish, B. Xu, H. Jin, Y. Y. Hu, G. Yu, J. B. Goodenough, *Angew. Chemie Int. Ed.* **2020**, *59*, 4131.
[48] I. Hanghofer, M. Brinek, S. L. Eisbacher, B. Bitschnau, M. Volck, V. Hennige, I. Hanzu, D. Rettenwander, H. M. R. Wilkening, *Phys. Chem. Chem. Phys.* **2019**, *21*, 8489.
[49] J. L. Ndeugueu, M. Aniya, *J. Phys. Soc. Japan* **2010**, *79*, 72.
[50] D. L. Sidebottom, *Rev. Mod. Phys.* **2009**, *81*, 999.
[51] S. Lunghammer, Q. Ma, D. Rettenwander, I. Hanzu, F. Tietz, H. M. R. Wilkening, *Chem. Phys. Lett.* **2018**, *701*, 147.
[52] L. Zhou, A. Assoud, A. Shyamsunder, A. Huq, Q. Zhang, P. Hartmann, J. Kulisch, L. F. Nazar, *Chem. Mater.* **2019**, *31*, 7801.
[53] Y. Gao, A. M. Nolan, P. Du, Y. Wu, C. Yang, Q. Chen, Y. Mo, S. H. Bo, *Chem. Rev.* **2020**, *120*, 5954.
[54] R. B. Nuernberg, *Ionics (Kiel)* **2020**, *26*, 2405.
[55] S. V. Patel, E. Truong, H. Liu, Y. Jin, B. L. Chen, Y. Wang, L. Miara, R. Kim, Y. Y. Hu, *Energy Storage Mater.* **2022**, *51*, 88.
[56] S. Muy, J. C. Bachman, H. H. Chang, L. Giordano, F. Maglia, S. Lupart, P. Lamp, W. G. Zeier, Y. Shao-Horn, *Chem. Mater.* **2018**, *30*, 5573.
[57] D. L. Sidebottom, *Phys. Rev. Lett.* **1999**, *83*, 983.
[58] F. Han, A. S. Westover, J. Yue, X. Fan, F. Wang, M. Chi, D. N. Leonard, N. J. Dudney, H. Wang, C. Wang, *Nat. Energy* **2019**, *4*, 187.
[59] S. Sarkar, V. Thangadurai, *ACS Energy Lett* **2022**, *7*, 1492.
[60] Y. Tian, T. Shi, W. D. Richards, J. Li, J. C. Kim, S. H. Bo, G. Ceder, *Energy Environ. Sci.* **2017**, *10*, 1150.
[61] F. Han, Y. Zhu, X. He, Y. Mo, C. Wang, *Adv. Energy Mater.* **2016**, *6*, 1501590.
[62] T. Swamy, X. Chen, Y. M. Chiang, *Chem. Mater.* **2019**, *31*, 707.
[63] T. Hakari, M. Deguchi, K. Mitsuhara, T. Ohta, K. Saito, Y. Orikasa, Y. Uchimoto, Y. Kowada, A. Hayashi, M. Tatsumisago, *Chem. Mater.* **2017**, *29*, 4768.
[64] R. Koerver, F. Walther, I. Aygün, J. Sann, C. Dietrich, W. G. Zeier, J. Janek, *J. Mater. Chem. A* **2017**, *5*, 22750.
[65] L. Sang, R. T. Haasch, A. A. Gewirth, R. G. Nuzzo, *Chem. Mater.* **2017**, *29*, 3029.
[66] D. Y. Oh, Y. E. Choi, D. H. Kim, Y.-G. Lee, B.-S. Kim, J. Park, H. Sohn, Y. S. Jung, *J. Mater. Chem. A* **2016**, *4*, 10329.
[67] B. R. Shin, Y. J. Nam, J. W. Kim, Y.-G. Lee, Y. S. Jung, *Sci. Rep.* **2015**, *4*, 5572.
[68] P. Minnmann, L. Quillman, S. Burkhardt, F. H. Richter, J. Janek, *J. Electrochem. Soc.* **2021**, *168*, 040537.
[69] K. Kaup, J. D. Bazak, S. H. Vajargah, X. Wu, J. Kulisch, G. R. Goward, L. F. Nazar, *Adv. Energy Mater.* **2020**, *10*, 1902783.
[70] P. E. Blöchl, *Phys. Rev. B* **1994**, *50*, 17953.
[71] G. Kresse, J. Furthmüller, *Phys. Rev. B* **1996**, *54*, 11169.
[72] J. P. Perdew, K. Burke, M. Ernzerhof, *Phys. Rev. Lett.* **1996**, *77*, 3865.
[73] J. Klimes, D. R. Bowler, A. Michaelides, *J. Phys. Condens. Matter* **2009**, *22*, 022201.
[74] J. Klimeš, D. R. Bowler, A. V. D. Michaelides, *Phys. Rev. B* **2011**, *83*, 195131.
[75] S. P. Ong, W. D. Richards, A. Jain, G. Hautier, M. Kocher, S. Cholia, D. Gunter, V. L. Chevrier, K. A. Persson, G. Ceder, *Comput. Mater. Sci.* **2013**, *68*, 314.
[76] Z. Deng, Z. Zhu, I. H. Chu, S. P. Ong, *Chem. Mater.* **2017**, *29*, 281.
[77] A. Jain, S. P. Ong, G. Hautier, W. Chen, W. D. Richards, S. Dacek, S. Cholia, D. Gunter, D. Skinner, G. Ceder, K. A. Persson, *APL Mater.* **2013**, *1*, 11002.
[78] S. P. Ong, S. Cholia, A. Jain, M. Brafman, D. Gunter, G. Ceder, K. A. Persson, *Comput. Mater. Sci.* **2015**, *97*, 209.
[79] G. Bergerhoff, R. Hundt, R. Sievers, I. D. Brown, *J. Chem. Inf. Comput. Sci.* **1983**, *23*, 66.
[80] C. J. Pickard, F. Mauri, *Phys. Rev. B* **2001**, *63*, 245101.
[81] J. R. Yates, C. J. Pickard, F. Mauri, *Phys. Rev. B* **2007**, *76*, 024401.
[82] P.-H. Chien, X. Feng, M. Tang, J. T. Rosenberg, S. O'neill, J. Zheng, S. C. Grant, Y. Y. Hu, *J. Phys. Chem. Lett.* **2018**, *9*, 1990.
[83] J. M. Doux, H. Nguyen, D. H. S. Tan, A. Banerjee, X. Wang, E. A. Wu, C. Jo, H. Yang, Y. S. Meng, *Adv. Energy Mater.* **2020**, *10*, 1903253.
[84] J. E. Trevey, C. R. Stoldt, S.-H. Lee, *J. Electrochem. Soc.* **2011**, *158*, A1282.